Replay as wavefronts and theta sequences as bump oscillations in a grid cell attractor network

Louis Kang[1,*] and Michael R. DeWeese[1]

[1] *Redwood Center for Theoretical Neuroscience, Helen Wills Neuroscience Institute, and Department of Physics, University of California, Berkeley, Berkeley, California, USA*

(Dated: March 1, 2019)

Grid cells fire in sequences that represent rapid trajectories in space. During locomotion, theta sequences encode sweeps in position starting slightly behind the animal and ending ahead of it. During quiescence and slow wave sleep, bouts of synchronized activity represent long trajectories called replays, which are well-established in place cells and have been recently reported in grid cells. Theta sequences and replay are hypothesized to facilitate many cognitive functions, but their underlying mechanisms are unknown. A leading mechanism proposed for grid cell formation is the continuous attractor network. We demonstrate that this established architecture naturally produces theta sequences and replay as distinct consequences of modulating external input. Driving inhibitory interneurons at the theta frequency causes attractor bumps to oscillate in speed and size, which gives rise to theta sequences and phase precession, respectively. Decreasing input drive to all neurons produces traveling wavefronts of activity that are decoded as replays.

The hippocampal region contains spatially tuned cells that generally encode an animal's position in its spatial environment. Place cells in the hippocampus proper fire at one or a few locations [1], and grid cells in the medial entorhinal cortex (MEC) fire at many locations that form a triangular lattice in space [2]. However, at short timescales, these neurons fire in coordinated sequences that represent trajectories away from the current animal position.

The first type of sequence occurs when the animal is moving and the local field potential (LFP) of the hippocampal region is dominated by an oscillation of 5–11 Hz, the theta range [3–5]. During every cycle of this oscillation, neurons corresponding to locations slightly behind the animal fire first, followed by those corresponding to the current location and finally locations ahead of the animal [6, 7]. These so-called theta sequences involving many neurons are related to a single-neuron phenomenon called phase precession [8, 9]. When an animal first enters the firing field of a place or grid cell, the neuron spikes late in the theta cycle. As the animal moves through the field, subsequent spikes tend to arrive at smaller theta phase, or earlier within a cycle. Thus, activity within each theta cycle starts with neurons whose peak firing occurs behind the animal and ends with neurons whose peak firing occurs ahead of the animal, which is a theta sequence [6].

The second type of sequence occurs when the animal is quietly awake and not moving, a state called quiescence; it also occurs during slow wave sleep, which will not concern us here. The LFP of the hippocampal region loses theta oscillations but is instead intermittently punctuated by sharp-wave ripples with power across 140–200 Hz [10, 11]. During these ripples, spatially tuned neurons fire in coordinated bursts that represent rapid, long-distance trajectories. These replays are well-established in place cells [12, 13] and have recently been observed in grid cells within superficial layers of the MEC [7]. Note that replays can also involve grid cells within *deep* layers of the MEC [14, 15]; these findings, which have been disputed [16], will not be addressed by this work.

Hippocampal experiments on theta sequences and replay have established a rich phenomenology, which includes their properties near branch points of a maze [17, 18], their modulation by reward history [19–22], their ability to predict future actions [23–26], and their potential role in disease pathogenesis [27]. These findings suggest that hippocampal sequences facilicate many cognitive functions, such as memory consolidation, credit assignment, and action planning [28–30]. However, the mechanisms that produce theta sequences and replay among place and grid cells are still unclear.

Meanwhile, a mechanism for producing grid cells themselves, the continuous attractor model, has been accumulating experimental support [31–37]. This class of networks posits particular configurations of synapses within the MEC that are local and symmetric [38, 39]. By incorporating key biological features such as fully spiking neural dynamics, we find that new phenomena emerge in this established recurrent architecture: grid cells will exhibit either theta sequences or replays depending on the external input provided by other brain regions. These inputs correspond to experimentally measured changes between active and inactive behavior [40, 41] and do not involve changes in connectivity. From this perspective, the same architecture that produces grid cells causes them to participate in sequences that may be leveraged by other brain regions, such as the hippocampus, to pursue desired cognitive goals.

* louis.kang@berkeley.edu

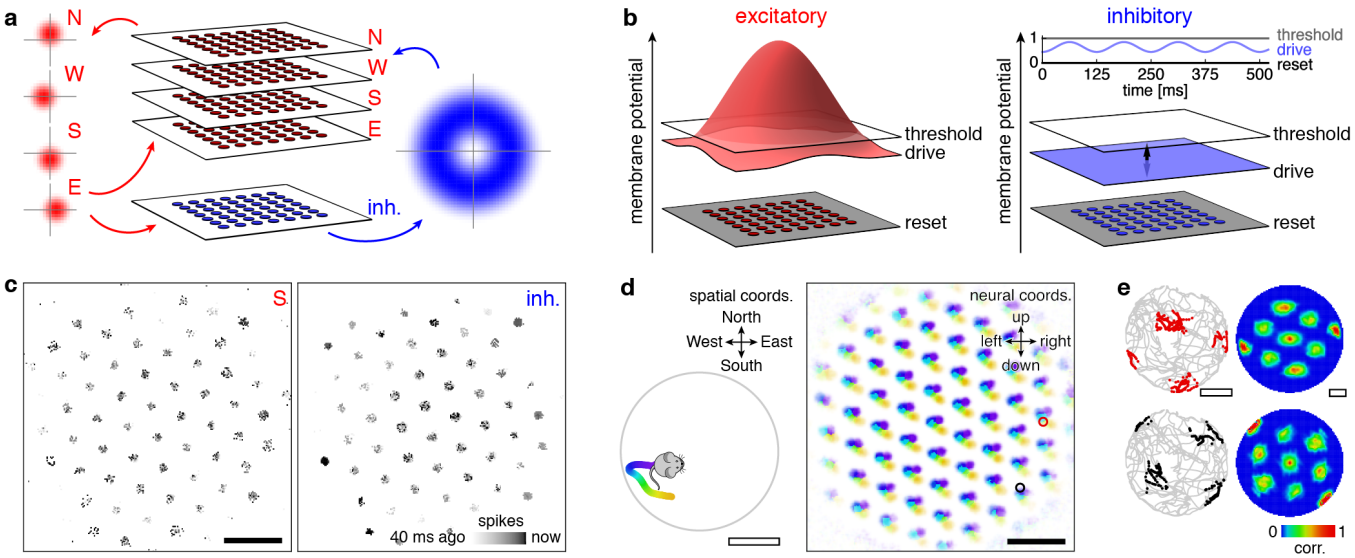

Figure 1. Model architecture and generation of 2D grid cells. (**a**) Our model consists of a neural sheet with five overlapping populations, four of them excitatory—N, W, S, and E—and one inhibitory. Each density plot depicts the synaptic outputs in the sheet of a neuron at the origin. (**b**) Each neuron is driven to a particular membrane potential, which exceeds the spiking threshold for excitatory neurons at the center of the sheet and oscillates at 8 Hz for inhibitory neurons. (**c**) Snapshot of neural activity showing S and inhibitory populations separately; other excitatory populations have activity patterns similar to that of the S population. Each pixel is a neuron and dark colors indicate recent spiking. (**d**) Left, segment of a 2D open field trajectory. Right, neural activity over the course of the segment with each neuron colored according to the position at which it attained its maximum firing rate. Each attractor bump moves in synchrony with animal motion. (**e**) Left, two sample grid cells with spikes shown as colored dots superimposed on the animal's trajectory. Each neuron's location in the sheet is indicated by a circle of corresponding color in **d**. Right, autocorrelation of rate maps calculated from spikes shown at left. Black scale bars, 50 neurons. White scale bars, 50 cm.

RESULTS

Our fully spiking continuous attractor model produces grid cells

We first describe our implementation of a continous attractor network and demonstrate that it reproduces classic grid responses when the simulated animal explores a 2D open field. Model details are provided in **Methods**. We simulate a single grid module—that is, grid cells of one scale and orientation [42]—with a continuous attractor network based on Refs. 38 and 39. Neurons are assembled in a 2D sheet with five overlapping populations, of which four represent excitatory principal cells and one represents inhibitory interneurons (**Fig. 1a**). Each excitatory neuron excites its neighbors across all populations, and each inhibitory neuron inhibits only excitatory neurons located a certain distance away. We will address the purpose of having four slightly different excitatory populations shortly.

To accurately simulate rapid sequences of spikes, we implement fully spiking grid cells that obey leaky integrate-and-fire dynamics. Each neuron has a membrane potential that tends toward a steady-state value called the drive, which represents a combination of resting potential and broad input from other brain regions (**Fig. 1b**). If the potential exceeds a threshold of 1 in arbitrary units, a spike is emitted, the potential is reset to 0, and the neuron's targets experience a postsynaptic jump in potential after a brief synaptic delay. During locomotion, excitatory principal cells are driven to fire by various neocortical and thalamic inputs [43]. Thus, their drive exceeds threshold at the center of the neural sheet; it decays towards the edges to avoid edge effects that disrupt continuous attractor dynamics [38]. Meanwhile, inhibitory interneurons have subthreshold drive that oscillates at a theta frequency of 8 Hz due to input from the medial septum [44–47]. With this architecture and random initial membrane potentials, the neural sheet naturally develops local regions of activity, called bumps, that are arranged in a triangular lattice and are coherent across populations (**Fig. 1c** and **Supp. Video 1**). This self-organized grid is an attractor state of the network.

How do we produce neurons with grid-like spatial tuning from the grid-like activity pattern on the neural sheet? This transformation is performed by the four excitatory populations, each of which corresponds to a perpendicular direction along the neural sheet and a perpendicular direction in the spatial environment. Excitatory neurons have output synapses biased in their preferred sheet direction (**Fig. 1a**), and they receive more input when the animal moves along their preferred spatial direction. When the animal moves along, say, the "North" direction, neurons in the N population have increased

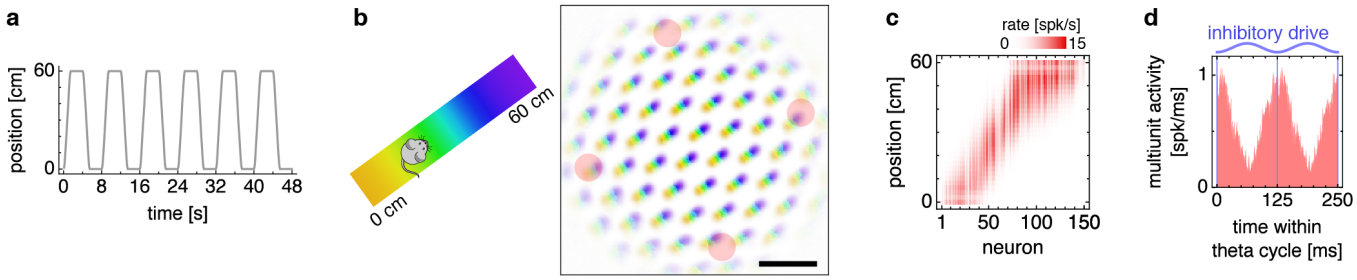

Figure 2. Grid cells along a 1D track. (**a**) Trajectory consisting of runs along a track separated by idle periods at either end. (**b**) Left, track diagram. Right, neural activity over trajectory runs with each neuron colored according to the position at which it attained maximum firing rate. Red circles indicate regions of recording. (**c**) Firing fields of recorded grid cells sorted by position of maximum rate. (**d**) Multiunit activity of neurons in **c** averaged over theta cycles, which span from one trough of the oscillating inhibitory drive to the next. Data is repeated over two cycles for clarity.

drive; since their outputs are biased in the "up" direction on the neural sheet, the activity pattern moves up. In this way, the activity pattern on the sheet moves synchronously with the animal's 2D trajectory (**Fig. 1d**), and the grid pattern is projected onto single neuron spatial responses (**Fig. 1e** and **Supp. Video 2**). Each active neuron in the sheet is a grid cell with the same scale and orientation.

Grid cells are spatially tuned and theta-modulated along a linear track

For the rest of the paper, we simulate 1D trajectories consisting of runs along a linear track separated by idle periods at either end (**Fig. 2a**). As in the 2D case, attractor bumps on the neural sheet move synchronously with animal motion, so grid cells at different locations in the sheet correspond to different positions along the track (**Fig. 2b**). From four regions in the sheet chosen for recording, we take up to 150 excitatory neurons whose spatial firing fields are stable from lap to lap (**Methods**) and collectively tile the track (**Fig. 2c** and **Supp. Fig. 1**). Unlike the 2D case in which grid cells have multiple firing fields, we choose parameters such that they have single fields to improve the intepretability of our results.

At the theta timescale, grid cell activity is highest when the oscillating inhibitory drive is lowest and excitatory cells are most disinhibited (**Fig. 2d**). This observation allows us identify theta phases in our simulations with those defined through LFP measurements. Experimentally, grid cells [9] and place cells [48, 49] are most active at troughs of the theta-filtered LFP, which can be explained in terms of extracellular currents generated by neural activity [50]. We will primarily compare our results to those of Ref. 7, who define theta cycles to span from trough to trough of the LFP. Accordingly, we align our theta cycles to start at troughs of the inhibitory drive (**Fig. 2d**).

Theta phase precession arises from oscillations in attractor bump size

During runs, activity passes through recorded neurons as attractor bumps move along the neural sheet (**Fig. 3a**, **Supp. Fig. 2**, and **Supp. Video 3**). However, spike trains from single neurons exhibit finer temporal organization with respect to the theta oscillation.

Certain grid cells prefer to fire at particular phases of the theta cycle (**Fig. 3b** and **Supp. Figs. 3** and **4**). For many of them, the preferred phase is 0°, when inhibitory drive is lowest and excitatory neurons are most disinhibited. For others, the preferred phase changes as the animal moves through the firing field. We quantify this behavior using circular-linear correlation, which indicates the presence of a preferred phase that varies linearly with position [51]. Out of the neurons that exhibit correlation (**Fig. 3c**), a small number exhibit large changes in preferred phase of magnitude $>10\,°/\text{cm}$ (**Fig. 3d**); their regression slope is negative for rightward laps and positive for leftward laps. This means that the preferred phase decreases as an animal traverses the firing field, a phenomenon known as theta phase precession, which has been observed classically in place cells [8] and more recently in grid cells [7, 9]. However, most of our simulated neurons have slopes close to 0, which indicates relatively constant preferred phases throughout the firing field (**Fig. 3d**). This is called phase locking and has also been observed in grid cells [7, 9].

We can understand the emergence of phase precession through the effect of oscillating inhibitory drive on attractor bumps. Higher inhibitory drive suppresses the activity of the excitatory grid cells and decreases the size, or effective diameter, of bumps (**Fig. 3e**, **f**). Imagine we record from a single neuron as a bump of activity moves through it on the neural sheet. As an attractor bump moves, its size oscillates with inhibitory drive (**Fig. 3g**, top, and **Supp. Video 4**). The activity bump will most likely first reach the grid cell when it is large and growing in size, which corresponds to the end of the theta cycle when the inhibitory drive is decreasing towards its

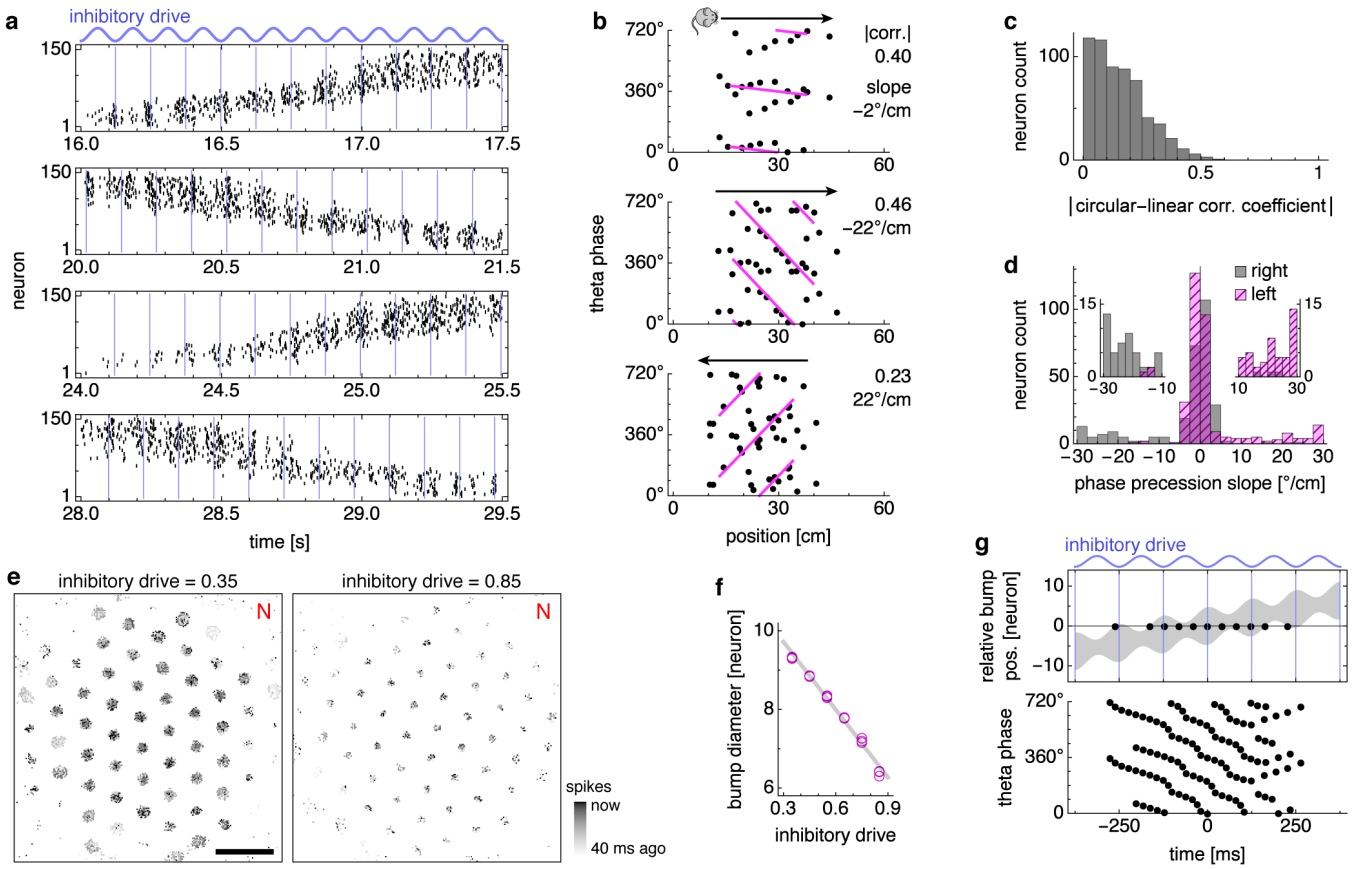

Figure 3. During runs, certain neurons exhibit theta phase precession due to bump size oscillations. (**a**) Grid cell spike rasters for four laps along the track. Vertical blue lines indicate theta cycle boundaries. (**b**) Relationship between animal position along the track and theta phase for three representative neurons. Dots represent spikes during runs in the directions indicated by arrows, with each spike repeated at two equivalent phases for clarity. Magnitudes of circular-linear correlation coefficients and slopes of fit lines obtained by circular-linear regression are indicated (right). (**c**) Magnitudes of circular-linear correlation coefficients for grid cells across all simulations. Mean ± s.d.: 0.15 ± 0.11. (**d**) Slopes of circular-linear regression lines for grid cells across all simulations. Runs to the right and left are plotted separately. Insets magnify regions of large slope with magnitude greater than $10\,^{\circ}$/cm; the predominance of negative values for rightward runs and positive for leftward runs indicates decreasing phase as the animal traverses grid fields in either direction. (**e**, **f**) Data from simulations with fixed inhibitory drive and constant animal velocity. (**e**) Snapshots of neural activity. Scale bar, 50 neurons. (**f**) The diameter of bumps on the neural sheet decreases linearly with increasing inhibitory drive. (**g**) Phase precession in a simplified conceptual model. We imagine an attractor bump, with size oscillations described by **f**, passing through a recorded grid cell. Top, a single lap. The recorded neuron is at position 0 and fires a spike (black dot) whenever contained within the bump (gray area), subject to a 40 ms refractory period. Bottom, relationship between theta phase and time across multiple laps in the same direction. Each lap starts with a different theta phase that uniformly samples the entire range. Theta phase generally decreases with time within in the grid field.

lowest point. Thus, as an animal enters a grid field, the first spike will likely have large theta phase slightly less than 360°. During the next theta cycle, the center of the bump has moved closer to the neuron, so the edge of the bump will reach the neuron when it is growing in size but not as large. Thus, the next spike will have slightly smaller theta phase. This is the origin of phase precession in our model. We continue generating spikes with simplified dynamics in which the neuron fires when it is contained within the bump, but there is a 40 ms refractory period corresponding to our model's membrane potential building up towards threshold after it is reset. The bump's movement through the recorded neuron represents one lap along the track at constant velocity.

We represent additional laps by performing the same simplified procedure as above, but with different shifts in theta phase, since the animal does not always enter the grid field at the same initial phase. Spikes accumulated across laps show phase precession (**Fig. 3g**, bottom, and **Supp. Video 4**), though the effect is strongest at the beginning of the field. In the middle of the field, spikes still precess, but they cluster around values of both 0° (equivalently, 360°) and 180°. At the end of the field, a few spikes even precess in the opposite direction, increas-

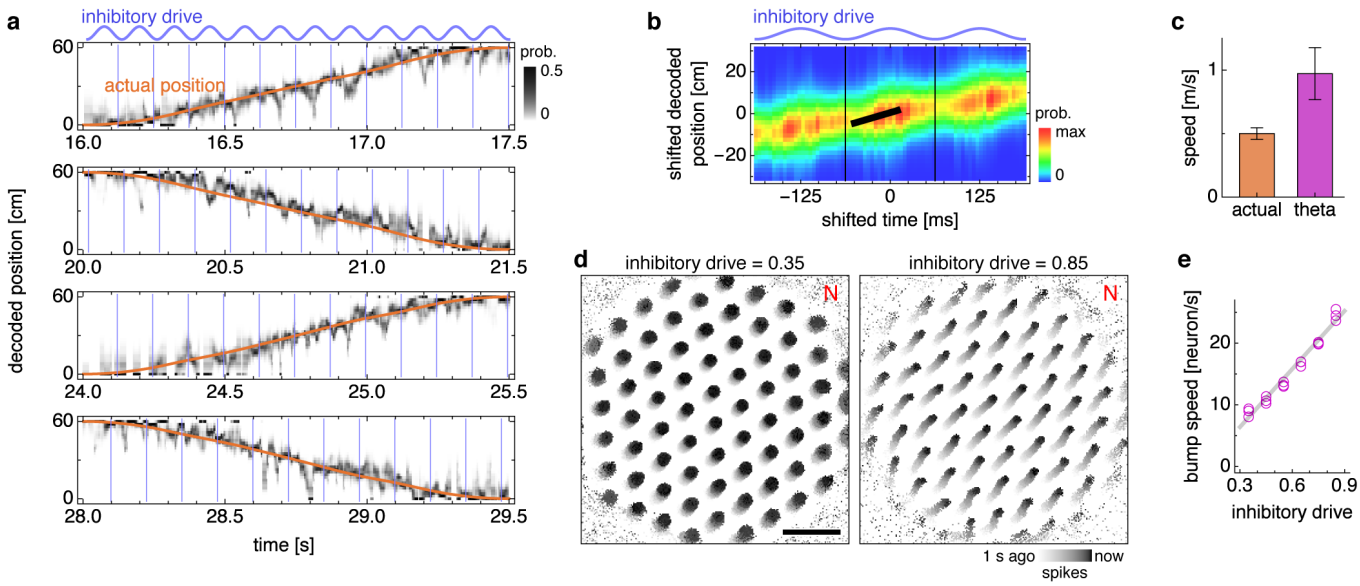

Figure 4. During runs, the decoded position exhibits theta sequences due to bump speed oscillations. (**a**) Decoded position for four laps along the track corresponding to **Fig. 3a**. Vertical blue lines indicate theta cycle boundaries. (**b**) Decoded position averaged over theta cycles. Thick black fit line indicates the time window with the steepest increase in decoded position. Vertical thin black lines indicate theta cycle boundaries. (**c**) Mean actual run speed (error bars indicate s.d. over time) and mean theta sequence speed, as indicated by the slope of the thick black line in **b** (error bars indicate s.d. over simulations). (**d**, **e**) Data from simulations with fixed inhibitory drive and constant animal velocity. (**d**) Snapshots of neural activity. Scale bar, 50 neurons. (**e**) The speed of bumps on the neural sheet increases linearly with inhibitory drive. Thus, the average decoded position in **b** advances most rapidly around the middle of the theta cycle.

ing in phase with time. Thus, bump oscillations alone can generate phase precession in our conceptual model with simplified spiking dynamics, but spike phases do not decrease perfectly linearly with progress through the field, which leads to our relatively low correlation values 0.15 ± 0.11 (mean $\pm$ s.d.; **Fig. 3c**). Experiments indicate higher correlation values in grid cells with mean $\approx$0.3, which is still less than the value $\approx$0.4 for place cells [7]. We mention in the **Discussion** electrophysiological features used by other models that can be added to our model to increase this correlation.

Theta sequences arise from oscillations in attractor bump speed

Now we use the firing fields illustrated in **Fig. 2c** to decode the animal's position from the population activity presented in **Fig. 3a** (**Methods**). The decoded position generally matches the animal's actual position (**Fig. 4a** and **Supp. Fig. 5**), but at the theta timescale, there are deviations whose regularities are revealed by averaging over theta cycles.

To do so, we take triplets of consecutive theta cycles, ignoring those whose decoded positions are close to the ends of the track and reversing those corresponding to right-to-left motion (**Methods**). We align the decoded positions with respect to the actual position of the animal midway through each theta triplet, and average these shifted decoded positions over theta triplets. This average decoded trajectory generally increases across the triplet, corresponding to the animal's actual forward motion (**Fig. 4b** and **Supp. Fig. 6**). However, at boundaries between theta cycles, the decoded position stalls, and toward the middle of each cycle, the decoded position increases rapidly. We identify these forward sweeps as theta sequences, which represent motion at 0.97 ± 0.20 m/s, approximately twice the actual speed of 0.50 ± 0.05 m/s (mean $\pm$ s.d.; **Fig. 4c**). This matches experimental observations of average theta sequence slope $\approx$1 m/s compared to the animal's speed of $\approx$0.4–0.5 m/s [7].

Theta sequences, like phase precession, arise naturally in our model from an effect of oscillating inhibitory drive on attractor bumps. In addition to determining bump size, inhibitory drive also affects the speed at which bumps move along the neural sheet—higher inhibitory drive produces faster bump motion for a given animal speed (**Fig. 3e**, **f**). At the middle of theta cycles, inhibitory drive is highest, so attractor bumps move quickly and represent fast animal trajectories. These theta sequences are faster than the animal's actual speed, which is approximately constant within a theta cycle and thus encoded as the average bump speed over the entire cycle.

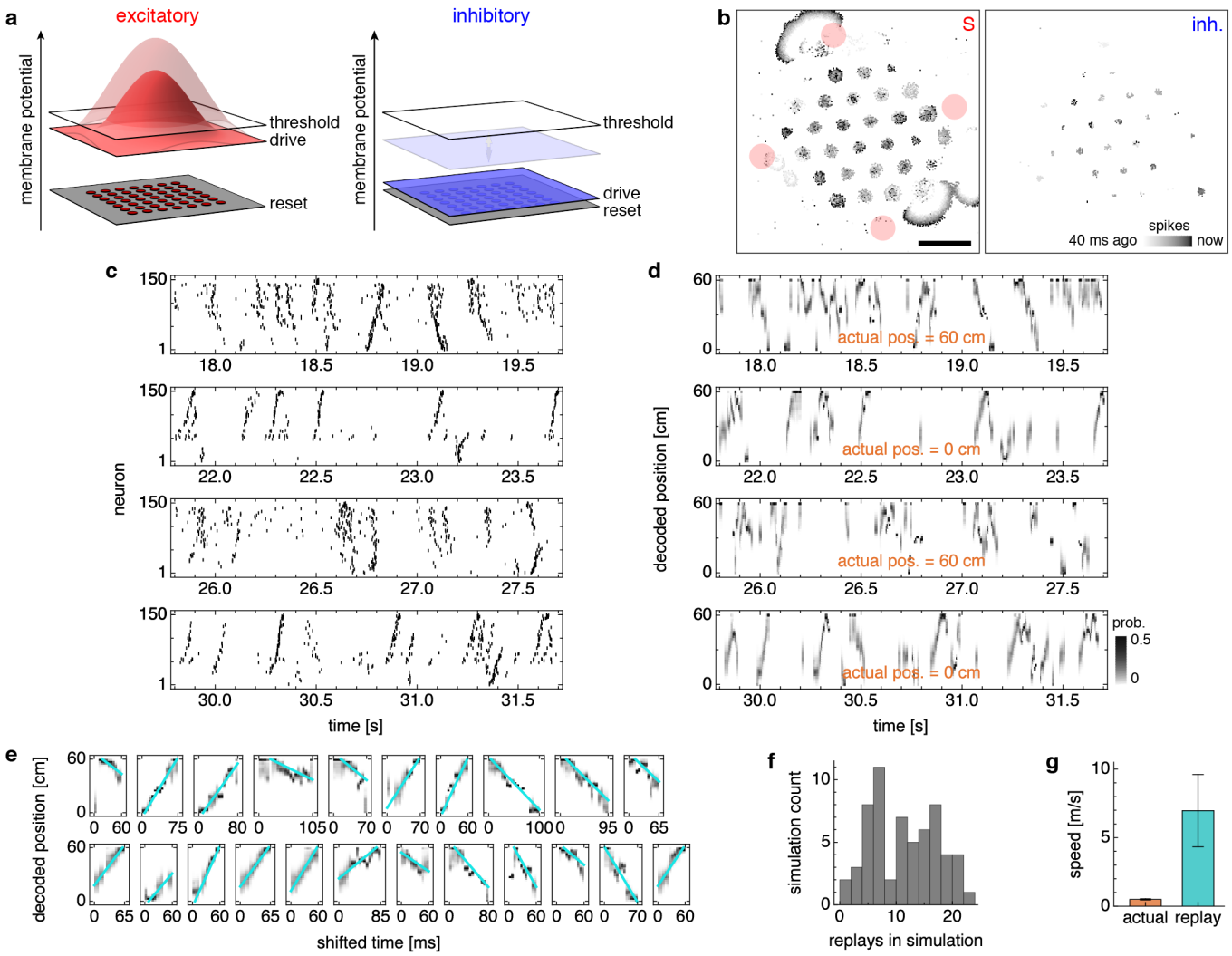

Figure 5. Lower drive during quiescence produces traveling wavefronts of activity that are decoded as replays. (**a**) During idle periods at either end of the track, excitatory and inhibitory drives decrease, and the latter no longer oscillates. (**b**) Snapshot of neural activity showing S and inhibitory populations separately. Red circles indicate regions of recording. Scale bar, 50 neurons. (**c**) Grid cell spike rasters for four quiescent periods. (**d**) Decoded position corresponding to **c**. Rapid trajectory sweeps arise from traveling wavefronts as depicted by the S population in **b**. (**e**) All replays from one simulation with cyan fit lines. (**f**) Number of replay events across simulations. (**g**) Mean actual run speed (error bars indicate s.d. over time) and mean replay speed, as indicated by the slopes of cyan lines in **e** (error bars indicate s.d. over replays).

Replay arises from traveling wavefronts of activity

We now simulate quiescent periods at either end of the track. We would like to know how external inputs to the MEC change at transitions between active and quiescent states, but these measurements have not been performed to our knowledge. Thus, we instead adapt experimental findings taken during slow wave sleep, which resembles the quiescent state in many behavioral and electophysiological ways [52]. The neocortex, which activates MEC principal cells, is broadly less active during slow wave sleep [40], and the medial septum, which inhibits MEC interneurons, increases its firing rate while losing most of its oscillatory nature [41]. We model these effects respectively as decreased excitatory drive and decreased inhibitory drive without oscillations (**Fig. 5a**). The network rapidly switches between these inputs and those of **Fig. 1a**, which represent the active state, as the animal transitions between quiescence and runs.

During quiescence, attractor bumps still form a lattice at the center of the neural sheet, where excitatory drive still exceeds threshold (**Fig. 5b** and **Supp. Video 3**). However, these bumps vanish toward the edge of the sheet, where they are replaced by traveling wavefronts of activity. These wavefronts cannot be solely sustained by excitatory drive, which is subthreshold in this outer region; instead, they must be nucleated and then self-sustained through excitatory-to-excitatory

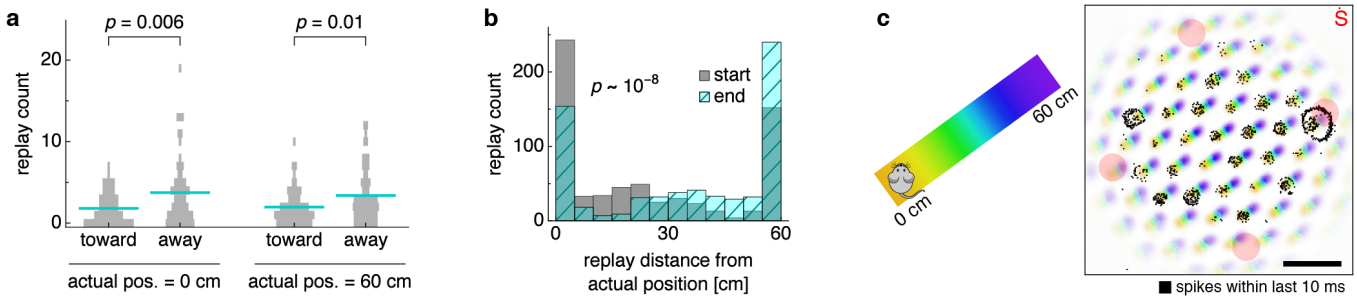

Figure 6. Replays preferentially propagate away from the actual animal position due to nucleation of wavefronts at attractor bumps. (**a**) Directions of replay propagation across simulations. For each actual position and replay direction, width of gray bars indicates the number of simulations with a particular replay count. Means indicated with lines. p-values from Mann-Whitney U tests show that a significantly greater number of replays propagate away from either actual position. (**b**) Start and end replay distances relative to the actual animal position. Paired medians compared by Wilcoxon rank-sum test with indicated p-value. (**c**) Left, track diagram with animal idle at 0 cm. Right, corresponding snapshot of neural activity superimposed on a background colored according to the position at which each neuron attains its maximum firing rate (**Fig. 2b**, right panel). Red circles indicate regions of recording. Attractor bumps still represent the animal position, and a wavefront can be seen emanating from one bump at the right. Scale bar, 50 neurons.

connections. In our model, nucleation occurs at activity bumps toward the edge of the sheet (**Fig. 5b** and **Supp. Video 3**). Once nucleated, the wavefront propagates freely through the outer region because inhibitory neurons, with low drive, are not activated by the wavefront. In contrast, wavefronts cannot propagate in the center region, because excitatory neurons there receive enough drive to spike vigorously and activate nearby inhibitory neurons (**Fig. 5b**, inhibitory population). These interneurons, with their surround distribution of synaptic outputs (**Fig. 1a**), constrain neural activity to localized bumps and prevent wavefront propagation.

When a wavefront passes through a region of recorded neurons, it appears as a sequence of spikes (**Fig. 5c** and **Supp. Fig. 7**) that is decoded as a rapid trajectory (**Fig. 5d** and **Supp. Fig. 8**). We identify these events as replays, which can traverse much of the track over ∼100 ms (**Fig. 5e** and **Supp. Fig. 9**). Due to the stochastic nature of wavefront generation, the number of detected replays varies considerably across laps within a simulation (**Fig. 5c, d**) and across replicate simulations (**Fig. 5f**). Nevertheless, decoded replays have a characteristic speed determined by that of wavefront propagation; it is 7.0 ± 2.6 m/s, which is about 14 times faster than the actual speed of 0.50 ± 0.05 m/s (mean ± s.d.; **Fig. 5g**). This agrees with experiments which measure replays at ≈4–6 m/s and actual motion at ≈0.4–0.5 m/s [7].

Replays in our model have a preferred direction of propagation; their decoded position tends to start near the actual position of the animal and travel away from it (**Fig. 6a**). Accordingly, replay start positions are closer to the actual location than end positions are (**Fig. 6b**). This directional bias has not been directly assessed for grid cells, but it appears in experiments on hippocampal replay [53, 54]. In our model, this effect is caused by the nucleation of replays at attractor bumps. When an animal is quiescent at either end of the track, attractor bumps are still located at neurons that represent the current position (**Fig. 6c** and **Supp. Video 5**). As a wavefront radiates from a bump, it will likely first activate neurons whose firing fields represent nearby positions, followed by those with increasingly distant fields. However, replays are not all detected immediately after wavefront nucleation; wavefronts traveling for some time may pass through a region of recorded neurons from any direction. Thus, despite the predominance of replays directed away from the actual animal position, some start at the opposite side of the track and travel toward the actual position (**Fig. 6a**).

DISCUSSION

Decades of hippocampal experiments have established theta phase precession, theta sequences, and replay as central features of place cell dynamics [4, 6, 10, 12, 13]. Evidence has been accumulating that grid cells, discovered more recently, exhibit the same phenomena [7, 9, 14]. These phenomena appear to be similar or interrelated in many ways, but experiments have also demonstrated important discordances. Theta sequences across place or grid cells with overlapping fields have been understood as the direct consequence of individually phase-precessing neurons [6, 8]. However, place cell experiments show that phase precession can appear without theta sequences [49]. Theta sequences and replays both represent temporally compressed trajectories and both seem important for memory consideration and planning [30, 55]. Yet, replay trajectories are significantly faster than theta sequences, and theta sequences only propagate in the direction of motion whereas replays can propagate in any direction relative to the resting animal [7, 49, 54, 56].

We unify phase precession, theta sequences, and re-

play under a single model while maintaining distinctions among them. Phase precession and theta sequences arise naturally from oscillations in attractor bump size and speed, respectively, which are both consequences of medial septum input. However, bump size and speed are not generally correlated across changes in other model parameters (**Supp. Fig. 10**). Thus, it is conceivable that one theta-related phenomenon can exist without the other under certain simulated or experimental conditions. Replays in our model arise from the disappearance of attractor bumps and their replacement by traveling wavefronts of activity. Wavefront propagation involves dynamical processes that are fundamentally different from attractor bump motion, and thus leads to different decoded speeds and directions for replays and theta sequences.

Crucially, we produce these phenomena in a continuous attractor network that can still generate 2D grid cells through path integration. Our implementation shares similarities with a classic version of the model [38] and a version whose connectivity can be learned [39]. However, there are three key differences. First, we use fully spiking neurons, which are rare in grid cell attractor models—we have only found them reported in Refs. 57 and 58, the latter of which combines an attractor network with the oscillatory interference model for grid cells [59, 60]. Typically, neural dynamics are founded on firing rates, which can be used to generate spike trains through a memoryless Poisson process [38, 39]; these models do not capture short time correlations between spikes that exist with our more realistic dynamics. Second, we include excitatory-to-excitatory connections in accordance with their recent experimental discovery [35, 36, 61, 62]. These connections allow wavefronts to propagate among excitatory neurons while nearby inhibitory neurons remain silent. Third, we vary the external input to the network between active and quiescent behavioral states in accordance with observations [40, 41]. Consequently, the network can instantly switch between operating regimes that exhibit either theta-related phenomena or replays.

Our model presents a distinct conception of entorhinal replay that can be tested experimentally. Direct observation of propagating wavefronts can be pursued by calcium imaging of the MEC [33, 37]. Otherwise, tetrode recordings of grid cell replay in open field environments may be analyzed for wavefront dynamics. In two dimensions, wavefronts would not represent a single trajectory, but instead a manifold of positions that sweep out a plane through space. New decoding techniques that do not assume that the grid cell population represents only one location at any given time would be required to distinguish between these two possible representations of motion.

We chose to build a continuous attractor model that can produce theta-related behavior and replay with as simple an architecture as possible, but we imagine that more complex network geometries are possible. For example, during quiescence, our model maintains activity bumps at the center of network and only exhibits replays at the edges; in the MEC, multiple areas may contain persistent attractor bumps that nucleate wavefronts. We have also ignored other known components of the grid system. We do not model multiple grid modules [42]. During runs, spike frequency adaptation [63] would reduce the number of spikes late in the grid field, which should enhance phase precession according to the conceptual model presented in **Fig. 3g** and **Supp. Video 4**. During quiescence, the MEC exhibits Up and Down states marked by high and low levels of activity; perhaps transitions between these states, which is associated with CA1 ripples [64], can nucleate multiple wavefronts that propagate in synchrony. Moreover, implementing connections to border [65, 66] or landmark cells [67, 68], which are thought to correct errors in path-integration [69], would remove any undesired lattice drift caused by wavefronts. This allocentric input can also remove the need for attractor bumps that persist through quiescence and maintain the animal's current position; instead, wavefronts may be free to propagate throughout the entire network.

Other models have been proposed for theta phase precession [70–72] and replay [73–78]. For example, one grid cell model uses after-spike depolarization within a 1D continuous attractor network to generate phase precession and theta sequences [71]. This experimentally observed feature pulls attractor bumps back to recently active locations every theta cycle. This could be added to our model to strengthen theta-related phenomena, but it is not required. Previously proposed replay models all intend to address place cells, not grid cells. Several of them encode replay trajectories into synaptic weights, either through hard-wiring or a learning mechanism [76–78]. Two models have suggested that replays originate from wavefronts of activity propagating through networks of place cells [73, 75]. These wavefronts then enhance connections through the network though spike-timing-dependent plasticity rules, which could account for the ability of reward to modulate hippocampal replay [21, 23].

Although our model also generates replay through activity wavefronts, it proposes a different paradigm for replay in the hippocampal region. First, our neurons are grid cells and must continue to function as such amid replays. Performing path integration in a continuous attractor model requires recurrent connectivity to be highly symmetric. Thus, replays should not signficantly alter synaptic strengths in the network; in our model, there is no alteration because we do not implement synaptic plasticity at all. And since our model does not require learning to produce replay, we can easily account for the observation of robust replays immediately after the first lap in a new track [13]. Otherwise, a strong learning mechanism must be invoked, which would continually distort synaptic symmetry.

Grid cells are thought to provide a spatial representation that is immediately available upon entering an environment and that remains stable over days of experi-

ence [2, 79, 80]. They provide spatial information to the hippocampus [81, 82], whose place cells associate location with environmental context [83, 84] and reward [85, 86] to aid the animal in pursuing its goals. In this vein, we envision that replay in superficial MEC layers acts as a pattern generator of many trajectories in space, which are presented to the hippocampus to be refined by experience and modulated by reward. The concept that sequences in hippocampus arise from superficial MEC layers has been experimentally substantiated for theta phenomena: lesioning the MEC disrupts phase precession and theta sequences in place cells [87], but grid cell phase precession is not affected by hippocampal inactivation [9].

Driving place cell replays with grid cell replays would require temporal coordination between the two, for which experimental support is mixed. Reference 7 does not find coordination between grid cell replays and ripples in CA1, but Ref. 88 reports that CA1 ripples are preceded by ripples in superficial MEC layers; further investigation would help resolve this discrepancy. Moreover, place cell activity appears to contain an abundance of certain short sequences that represent contiguous locations in novel environments and participate frequently in replays [89]; this finding is related to the disputed [90] observation of hippocampal preplay [91–93]. From the perspective of our model, such preexisting sequences may arise from wavefronts generated intrinsically by grid cells, which then drive corresponding place cells. After experience, hippocampal plasticity supplements the sequences with additional place cells to enhance their representation of meaningful trajectories [92]. In this way, wavefronts in the MEC can accelerate learning by providing a scaffold for the hippocampus to modify and improve. Meanwhile, the MEC maintains a symmetric representation of space, so the next experience, possibly with different spatial properties, can be learned equally well.

ACKNOWLEDGMENTS

The authors thank John Widloski, David Foster, Fritz Sommer, Zengyi Li, Guy Isely, Kate Jeffery, and Hugo Spiers for stimulating discussions. L. K. is supported by the Miller Institute for Basic Research in Science, and M. R. D. is partly supported by the Army Research Office through grant W911NF-13-1-0390. Part of this work was performed at the Simons Institute for the Theory of Computing.

METHODS

This section provides an overview of our simulation methods. Full details are provided in **Supp. Info.**

Table 1. Main model parameters and their values unless otherwise noted. Values that change between runs along the track and idle periods at either end are indicated accordingly.

Parameter	Variable	Value
Neurons per population	$n \times n$	232×232
Simulation timestep	Δt	1 ms
Exc. membrane time constant	τ_{m}^{+}	40 ms
Inh. membrane time constant	τ_{m}^{-}	20 ms
Exc.-to-exc. synaptic delay	τ_{s}^{++}	5 ms
Exc.-to-inh. synaptic delay	τ_{s}^{-+}	2 ms
Inh. synaptic delay	τ_{s}^{-}	2 ms
Exc. drive maximum	a_{max}^{+}	$\begin{cases} 2.0 & \text{runs} \\ 1.6 & \text{idle} \end{cases}$
Exc. drive minimum	a_{min}^{+}	0.8
Exc. drive scaled spread	ρ_{a^+}	$\begin{cases} 1.2 & \text{runs} \\ 0.9 & \text{idle} \end{cases}$
Inh. drive magnitude	a_{mag}^{-}	$\begin{cases} 0.65 & \text{runs} \\ 0.1 & \text{idle} \end{cases}$
Inh. drive theta amplitude	a_{th}^{-}	$\begin{cases} 0.2 & \text{runs} \\ 0 & \text{idle} \end{cases}$
Inh. drive theta frequency	f	8 Hz
Exc. synaptic strength	w_{mag}^{+}	0.2
Exc. synaptic spread	r_{w^+}	6
Inh. synaptic strength	w_{mag}^{-}	2.8
Inh. synaptic distance	r_{w^-}	12
Exc. synaptic shift	ξ	2
Exc. velocity gain	α	0.12 s/m
Exc. noise magnitude	$\mathrm{Var}[\zeta^P(\mathbf{r},t)]$	0.012^2
Inh. noise magnitude	$\mathrm{Var}[\zeta^-(\mathbf{r},t)]$	0.012^2

Model architecture and dynamics

Our architecture is inspired by Refs. 38 and 39. A 2D neural sheet contains five overlapping populations, each with neurons at $\mathbf{r} = (x, y)$, where $x = 1, \ldots, n$ and $y = 1, \ldots, n$. There are four excitatory populations: N, S, W, and E; we index them by P and use the symbol $+$ for parameters common to all of them. There is one inhibitory population $-$.

Each excitatory neuron is described by a membrane potential $\phi^P(\mathbf{r}, t)$ and a spike indicator $s^P(\mathbf{r}, t)$, which equals either 1 if neuron $\mathbf{r}$ in population P spiked at time t or 0 otherwise. When the potential exceeds a threshold of 1 in arbitrary units, the neuron fires a spike and its potential is reset to 0:

$$\phi^P(\mathbf{r}, t) \leftarrow 0 \quad \text{and} \quad s^P(\mathbf{r}, t) \leftarrow 1. \tag{1}$$

We prevent $\phi^P(\mathbf{r}, t)$ from decreasing past -1 as a limit on hyperpolarization. The same definitions and dynamics apply to the inhibitory population $-$.

Membrane potentials follow leaky integrator dynamics.

The excitatory neurons obey

$$\begin{aligned}\tau_{\mathrm{m}}^{+}\frac{\phi^{P}(\mathbf{r},t+\Delta t)-\phi^{P}(\mathbf{r},t)}{\Delta t}+\phi^{P}(\mathbf{r},t)\\ =\sum_{P',\mathbf{r}'}w^{+}(\mathbf{r}-\mathbf{r}'-\xi\hat{\mathbf{e}}^{P'})s^{P'}(\mathbf{r}',t-\tau_{\mathrm{s}}^{++})\\ +\sum_{\mathbf{r}'}w^{-}(\mathbf{r}-\mathbf{r}')s^{-}(\mathbf{r}',t-\tau_{\mathrm{s}}^{-})\\ +a^{+}(\mathbf{r})\left[1+\alpha\hat{\mathbf{E}}^{P}\cdot\mathbf{V}(t)\right]+\zeta^{P}(\mathbf{r},t).\end{aligned}\tag{2}$$

And the inhibitory neurons obey

$$\begin{aligned}\tau_{\mathrm{m}}^{-}\frac{\phi^{-}(\mathbf{r},t+\Delta t)-\phi^{-}(\mathbf{r},t)}{\Delta t}+\phi^{-}(\mathbf{r},t)\\ =\sum_{P',\mathbf{r}'}w^{+}(\mathbf{r}-\mathbf{r}'-\xi\hat{\mathbf{e}}^{P'})s^{P'}(\mathbf{r}',t-\tau_{\mathrm{s}}^{-+})\\ +a^{-}(\mathbf{r},t)+\zeta^{-}(\mathbf{r},t).\end{aligned}\tag{3}$$

Neural drive is given by a, which is modulated by the animal's velocity $\mathbf{V}(t)$ for excitatory neurons. Each excitatory population P prefers a perpendicular direction in space $\hat{\mathbf{E}}^{P}$, which we call North, South, West, and East for the populations N, S, W, and E. Neural connectivity is given by w. Each excitatory population P has its synaptic outputs shifted by a small amount ξ in a preferred direction $\hat{\mathbf{e}}^{P}$ on the neural sheet, which we call up, down, left, and right for the populations N, S, W, and E. Spikes produce an instantaneous change in postsynaptic membrane potential after a synaptic delay τ_{s}, which is longer for excitatory-to-excitatory connections (τ_{s}^{++}) than for excitatory-to-inhibitory connections (τ_{s}^{-+}) based on axon morphology [62]. Independent, zero-mean, normally distributed noise ζ is added to each neuron at each timestep.

See **Table 1** for complete variable definitions and values.

Drive and connectivity

The drive to excitatory populations is

$$a^{+}(\mathbf{r})=\begin{cases}a_{\min}^{+}+(a_{\max}^{+}-a_{\min}^{+})\dfrac{1+\cos(\pi\rho/\rho_{a^{+}})}{2} & \rho<\rho_{a^{+}}\\ a_{\min}^{+} & \rho\geq\rho_{a^{+}},\end{cases}\tag{4}$$

where $\rho=\sqrt{\left(x-\frac{n+1}{2}\right)^{2}+\left(y-\frac{n+1}{2}\right)^{2}}\Big/\frac{n}{2}$ is a scaled radial distance for the neuron at $\mathbf{r}=(x,y)$. It equals 0 at the center of the neural sheet and approximately 1 at the midpoint of an edge. The drive to inhibitory subpopulations is

$$a^{-}(\mathbf{r},t)=a_{\mathrm{mag}}^{-}-a_{\mathrm{th}}^{-}\cos(2\pi ft+\psi_{0}),\tag{5}$$

where ψ_0 is a phase offset chosen randomly at the start of each lap.

The synaptic connectivity from excitatory neurons to all neurons is based on the symmetric function

$$w^{+}(\mathbf{r})=\begin{cases}w_{\mathrm{mag}}^{+}\dfrac{1+\cos(\pi r/r_{w^{+}})}{2} & r<r_{w^{+}}\\ 0 & r\geq r_{w^{+}},\end{cases}\tag{6}$$

where $r=|\mathbf{r}|$. The synaptic connectivity from inhibitory neurons to excitatory neurons is

$$w^{-}(\mathbf{r})=\begin{cases}-w_{\mathrm{mag}}^{-}\dfrac{1-\cos(\pi r/r_{w^{-}})}{2} & r<2r_{w^{-}}\\ 0 & r\geq 2r_{w^{-}}.\end{cases}\tag{7}$$

There is no connectivity from inhibitory neurons to other inhibitory neurons.

See **Table 1** for complete variable definitions and values.

Single neuron recording and decoding

We simulate our model 20 times with slightly different run trajectories randomly generated by fractional Brownian motion processes, followed by 20 more times with the same trajectories but reversed velocities. These simulations produce spike trains for all neurons in the network. To match multiunit tetrode recordings, we select two subsets containing up to 150 excitatory neurons in each simulation. Each of these subsets is an independent recording to be analyzed separately. We call each of these 80 recordings a "simulation" in our results.

We select neurons for recording as follows. For the first subset, we choose four points on the neural sheet whose distance from the center is 95 neurons and whose angular positions, or clock positions, are random but equally spaced. From circular areas of radius 12 centered at these points, we randomly select between 100 and 150 excitatory neurons whose firing fields are stable across laps. For the second subset, we choose the four circular areas with the same distance from the center of the sheet and with angular positions offset 45° from the first four areas. We again select 100–150 neurons with stable firing fields. If we are not able to select at least 100 neurons, we exclude the simulation from further analysis; 61 of the 80 simulations remain. All single-simulation results reported in this paper come from the same simulation.

We use grid cell firing fields accrued from all laps in both directions to decode the animal's position from the population activity of its recorded neurons. We use the standard Bayesian decoding procedure that assumes independent, Poisson-distributed spike counts and a uniform prior [7, 94].

[1] J. O'Keefe and J. Dostrovsky, Brain Res. **34**, 171 (1971).
[2] T. Hafting, M. Fyhn, S. Molden, M.-B. Moser, and E. I. Moser, Nature **436**, 801 (2005).
[3] C. H. Vanderwolf, Electroencephalography and Clinical Neurophysiology **26**, 407 (1969).
[4] J. O'Keefe, Experimental Neurology **51**, 78 (1976).
[5] O. S. Vinogradova, Prog. Neurobiol. **45**, 523 (1995).
[6] W. E. Skaggs, B. L. McNaughton, M. A. Wilson, and C. A. Barnes, Hippocampus **6**, 149 (1996).
[7] J. O'Neill, C. N. Boccara, F. Stella, P. Schoenenberger, and J. Csicsvari, Science **355**, 184 (2017).
[8] J. O'Keefe and M. L. Recce, Hippocampus **3**, 317 (1993).
[9] T. Hafting, M. Fyhn, T. Bonnevie, M.-B. Moser, and E. I. Moser, Nature **453**, 1248 (2008).
[10] G. Buzsáki, Brain Res. **398**, 242 (1986).
[11] J. J. Chrobak and G. Buzsáki, J. Neurosci. **16**, 3056 (1996).
[12] A. K. Lee and M. A. Wilson, Neuron **36**, 1183 (2002).
[13] D. J. Foster and M. A. Wilson, Nature **440**, 680 (2006).
[14] H. F. Ólafsdóttir, F. Carpenter, and C. Barry, Nat. Neurosci. **19**, 792 (2016).
[15] H. F. Ólafsdóttir, F. Carpenter, and C. Barry, Neuron **96**, 925 (2017).
[16] J. B. Trimper, S. G. Trettel, E. Hwaun, and L. L. Colgin, Front. Syst. Neurosci. **11**, 39 (2017).
[17] X. Wu and D. J. Foster, J. Neurosci. **34**, 6459 (2014).
[18] H. Belchior, V. L. dos Santos, A. B. L. Tort, and S. Ribeiro, Hippocampus **24**, 693 (2014).
[19] A. Johnson and A. D. Redish, J. Neurosci. **27**, 12176 (2007).
[20] A. M. Wikenheiser and A. D. Redish, Curr. Opin. Neurobiol. **32**, 8 (2015).
[21] R. E. Ambrose, B. E. Pfeiffer, and D. J. Foster, Neuron **91**, 1124 (2016).
[22] C.-T. Wu, D. Haggerty, C. Kemere, and D. Ji, Nat. Neurosci. **20**, 571 (2017).
[23] B. E. Pfeiffer and D. J. Foster, Nature **497**, 74 (2013).
[24] A. C. Singer, M. F. Carr, M. P. Karlsson, and L. M. Frank, Neuron **77**, 1163 (2013).
[25] A. M. Wikenheiser and A. D. Redish, Nat. Neurosci. **18**, 289 (2015).
[26] H. Xu, P. Baracskay, J. O'Neill, and J. Csicsvari, Neuron (2018).
[27] S. J. Middleton, E. M. Kneller, S. Chen, I. Ogiwara, M. Montal, K. Yamakawa, and T. J. McHugh, Nat. Neurosci. **34**, 1 (2018).
[28] D. J. Foster, Annu. Rev. Neurosci. **40**, 581 (2017).
[29] H. F. Ólafsdóttir, D. Bush, and C. Barry, Current Biology **28**, R37 (2018).
[30] M. C. Zielinski, W. Tang, and S. P. Jadhav, Hippocampus **91**, 1124 (2018).
[31] J. J. Couey, A. Witoelar, S.-J. Zhang, K. Zheng, J. Ye, B. Dunn, R. Czajkowski, M.-B. Moser, E. I. Moser, Y. Roudi, and M. P. Witter, Nat. Neurosci. **16**, 318 (2013).
[32] K. Yoon, M. A. Buice, C. Barry, R. Hayman, N. Burgess, and I. R. Fiete, Nat. Neurosci. **16**, 1077 (2013).
[33] J. G. Heys, K. V. Rangarajan, and D. A. Dombeck, Neuron **84**, 1079 (2014).
[34] B. Dunn, M. Mørreaunet, and Y. Roudi, PLOS Comp. Biol. **11**, e1004052 (2015).
[35] E. C. Fuchs, A. Neitz, R. Pinna, S. Melzer, A. Caputi, and H. Monyer, Neuron **89**, 194 (2016).
[36] I. Zutshi, M. L. Fu, V. Lilascharoen, J. K. Leutgeb, B. K. Lim, and S. Leutgeb, Nat. Commun. **9**, 3701 (2018).
[37] Y. Gu, S. Lewallen, A. A. Kinkhabwala, C. Domnisoru, K. Yoon, J. L. Gauthier, I. R. Fiete, and D. W. Tank, Cell **175**, 736 (2018).
[38] Y. Burak and I. R. Fiete, PLOS Comp. Biol. **5**, e1000291 (2009).
[39] J. Widloski and I. R. Fiete, Neuron **83**, 481 (2014).
[40] M. Steriade, I. Timofeev, and F. Grenier, J. Neurophysiol. **85**, 1969 (2001).
[41] A. P. Simon, F. Poindessous-Jazat, P. Dutar, J. Epelbaum, and M.-H. Bassant, J. Neurosci. **26**, 9038 (2006).
[42] H. Stensola, T. Stensola, T. Solstad, K. Frøland, M.-B. Moser, and E. I. Moser, Nature **492**, 72 (2012).
[43] K. M. Kerr, K. L. Agster, S. C. Furtak, and R. D. Burwell, Hippocampus **17**, 697 (2007).
[44] M. P. Brandon, A. R. Bogaard, C. P. Libby, M. A. Connerney, K. Gupta, and M. E. Hasselmo, Science **332**, 595 (2011).
[45] J. Koenig, A. N. Linder, J. K. Leutgeb, and S. Leutgeb, Science **332**, 592 (2011).
[46] A. Gonzalez-Sulser, D. Parthier, A. Candela, C. McClure, H. Pastoll, D. Garden, G. Sürmeli, and M. F. Nolan, J. Neurosci. **34**, 16739 (2014).
[47] G. Unal, A. Joshi, T. J. Viney, V. Kis, and P. Somogyi, J. Neurosci. **35**, 15812 (2015).
[48] G. Buzsáki, Neuron **33**, 325 (2002).
[49] T. Feng, D. Silva, and D. J. Foster, J. Neurosci. **35**, 4890 (2015).
[50] G. Buzsáki, C. A. Anastassiou, and C. Koch, Nat. Rev. Neurosci. **13**, 407 (2012).
[51] R. Kempter, C. Leibold, G. Buzsáki, K. Diba, and R. Schmidt, Journal of Neuroscience Methods **207**, 113 (2012).
[52] G. Buzsaki, Cereb Cortex **6**, 81 (1996).
[53] K. Diba and G. Buzsáki, Nat. Neurosci. **10**, 1241 (2007).
[54] T. J. Davidson, F. Kloosterman, and M. A. Wilson, Neuron **63**, 497 (2009).
[55] D. J. Foster and J. J. Knierim, Curr. Opin. Neurobiol. **22**, 294 (2012).
[56] C. Zheng, K. W. Bieri, Y.-T. Hsiao, and L. L. Colgin, Neuron **89**, 398 (2016).
[57] G. English, *Spiking neural network models for the emergence of patterned activity in grid cell populations*, Master's thesis, ETH Zurich and University of Zurich, Switzerland (2017).
[58] D. Bush and N. Burgess, J. Neurosci. **34**, 5065 (2014).
[59] N. Burgess, C. Barry, and J. O'Keefe, Hippocampus **17**, 801 (2007).
[60] M. E. Hasselmo, L. M. Giocomo, and E. A. Zilli, Hippocampus **17**, 1252 (2007).
[61] J. Winterer, N. Maier, C. Wozny, P. Beed, J. Breustedt, R. Evangelista, Y. Peng, T. D'Albis, R. Kempter, and D. Schmitz, Cell Reports **19**, 1110 (2017).
[62] H. Schmidt, A. Gour, J. Straehle, K. M. Boergens, M. Brecht, and M. Helmstaedter, Nature **549**, 469 (2017).
[63] M. Yoshida, A. Jochems, and M. E. Hasselmo, PLOS

ONE **8**, e73904 (2013).
[64] T. T. G. Hahn, J. M. McFarland, S. Berberich, B. Sakmann, and M. R. Mehta, Nat. Neurosci. **15**, 1531 (2012).
[65] S. A. Ocko, K. Hardcastle, L. M. Giocomo, and S. Ganguli, Proc. Natl. Acad. Sci. U. S. A. **115**, E11798 (2018).
[66] A. T. Keinath, R. A. Epstein, and V. Balasubramanian, eLife **7**, 71 (2018).
[67] F. Raudies and M. E. Hasselmo, PLOS Comp. Biol. **11**, e1004596 (2015).
[68] F. Savelli, J. D. Luck, and J. J. Knierim, eLife **6**, 493 (2017).
[69] K. Hardcastle, S. Ganguli, and L. M. Giocomo, Neuron **86**, 827 (2015).
[70] M. V. Tsodyks, W. E. Skaggs, T. J. Sejnowski, and B. L. McNaughton, Hippocampus **6**, 271 (1996).
[71] Z. Navratilova, L. M. Giocomo, J.-M. Fellous, M. E. Hasselmo, and B. L. McNaughton, Hippocampus **22**, 772 (2012).
[72] K. Thurley, F. Hellmundt, and C. Leibold, Hippocampus **23**, 786 (2013).
[73] F. Ponulak and J. J. Hopfield, Front Comput Neurosci **7** (2013).
[74] A. H. Azizi, L. Wiskott, and S. Cheng, Front Comput Neurosci **7**, 161 (2013).
[75] M. Bayati, A. Valizadeh, A. Abbassian, and S. Cheng, Front Comput Neurosci **9**, 1178 (2015).
[76] N. Chenkov, H. Sprekeler, and R. Kempter, PLOS Comp. Biol. **13**, e1005359 (2017).
[77] L. Gönner, J. Vitay, and F. H. Hamker, Front Comput Neurosci **11**, 3 (2017).
[78] T. Haga and T. Fukai, eLife **7**, 1124 (2018).
[79] J. K. Leutgeb, S. Leutgeb, M. B. Moser, and E. I. Moser, Science **315**, 961 (2007).
[80] G. W. Diehl, O. J. Hon, S. Leutgeb, and J. K. Leutgeb, Hippocampus **17**, 71 (2018).
[81] S. Cheng and L. M. Frank, Neuroscience **197**, 293 (2011).
[82] J. B. Hales, M. I. Schlesiger, J. K. Leutgeb, L. R. Squire, S. Leutgeb, and R. E. Clark, Cell Reports **9**, 893 (2014).
[83] M. A. Wilson and B. L. McNaughton, Science (1993).
[84] M. I. Anderson and K. J. Jeffery, J. Neurosci. **23**, 8827 (2003).
[85] S. A. Hollup, S. Molden, J. G. Donnett, M.-B. Moser, and E. I. Moser, J. Neurosci. **21**, 1635 (2001).
[86] O. Mamad, L. Stumpp, H. M. McNamara, C. Ramakrishnan, K. Deisseroth, R. B. Reilly, and M. Tsanov, PLOS Biology **15**, e2002365 (2017).
[87] M. I. Schlesiger, C. C. Cannova, B. L. Boublil, J. B. Hales, E. A. Mankin, M. P. Brandon, J. K. Leutgeb, C. Leibold, and S. Leutgeb, Nat. Neurosci. **18**, 1123 (2015).
[88] J. Yamamoto and S. Tonegawa, Neuron **96**, 217 (2017).
[89] K. Liu, J. Sibille, and G. Dragoi, Neuron **0** (2018).
[90] D. Silva, T. Feng, and D. J. Foster, Nat. Neurosci. **18**, 1772 (2015).
[91] G. Dragoi and S. Tonegawa, Nature **469**, 397 (2011).
[92] A. D. Grosmark and G. Buzsáki, Science **351**, 1440 (2016).
[93] K. Liu, J. Sibille, and G. Dragoi, Hippocampus (2018).
[94] K. Zhang, I. Ginzburg, B. L. McNaughton, and T. J. Sejnowski, J. Neurophysiol. **79**, 1017 (1998).